The Thesis Committee for Sergio Andre Tovar
certifies that this is the approved version of the following thesis:

Simulation of LCROSS Hydroxyl Band Strength Data

APPROVED BY

SUPERVISING COMMITTEE:

David B. Goldstein, Supervisor

Philip L. Varghese, Co-Supervisor

Simulation of LCROSS Hydroxyl Band Strength Data

by

Sergio Andre Tovar

Thesis

Presented to the Faculty of the Graduate School of

The University of Texas at Austin

in Partial Fulfillment

of the Requirements

for the Degree of

Master of Science in Engineering

The University of Texas at Austin

May 2019

Dedicated to my friends.

Acknowledgments

I would like to express my deep gratitude to the whole Computational Fluid Physics Lab research group for their contributions to this project. In particular, thanks to professors Dr. David B. Goldstein, Dr. Philip L. Varghese, and Dr. Laurence M. Trafton for their continuous guidance, support, and for sharing their love of science with me and all of their students; to fellow research-group students Yasvanth Poondla and Aayush Agrawal, for their essential contributions to this work; and to Dr. Arnaud Mahieux for his continuous feedback and mentoring. Finally, thanks to collaborator Dr. Anthony Colaprete for providing the data utilized in this work, as well as helping in the analysis of the results.

Sergio Andre Tovar

The University of Texas at Austin

May 2019

Abstract

Simulation of LCROSS Hydroxyl Band Strength Data

Sergio Andre Tovar, M.S.E.

The University of Texas at Austin, 2019

Supervisor: David B. Goldstein

Co-Supervisor: Philip L. Varghese

In 2009, NASA launched the Lunar CRater Observation and Sensing Satellite (LCROSS) mission to confirm and characterize the presence of water ice in the Moon. This work aims to characterize the Moon's regolith by analysing LCROSS data not studied in detail before, the hydroxyl (OH) band strength observations. A simulated OH band strength was obtained by an improved numerical model based on previous work by Heldmann et al. (2015). Using a fitting method, we fitted three hypothesized OH-producing processes to the OH band strength data. Multiple solutions arose from the fitting method, and the models were only moderately constrained. The results indicate that a prompt release of OH is necessary to explain early data, and that most of the OH band signal after $\sim$ 15 seconds was produced by the photodissociation of water from ice-containing grains in the LCROSS impact-plume.

Contents

Acknowledgments **v**

Abstract **vi**

List of Tables **ix**

List of Figures **x**

Chapter 1 Introduction **1**

Chapter 2 LCROSS Mission Overview **4**

Chapter 3 Hydroxyl Band Strength Data **6**

Chapter 4 Simulation Code **9**

4.1 LCROSS simulation and improvements 9

4.1.1 Photodissociation model 10

4.1.2 Grain heating model 11

4.2 OH producing mechanisms 12

4.2.1 Mechanism 1: OH from grains 12

4.2.2 Mechanism 2: Sweating crater model for H_2O vapor production 16

4.2.3 Mechanism 3: Prompt OH directly evolving from the crater . 18

Chapter 5 Fitting Method **20**

5.1 Part I: Fitting the Hydroxyl Band Strength 21

5.1.1 Categorization of parameters 21

5.1.2 Discretization of the Parameter Space 23

5.1.3 Combining OH-Producing Mechanisms to Estimate Hydroxyl Band Strength Observations From Computational Results . . 25

5.1.4 Least-squares fit for a particular combination of curves 26

5.1.5 Testing all combinations of curves 27

5.2 Part II: Confidence intervals on the fit 29

Chapter 6 Results and Discussion **33**

6.1 Olivine Results 33

6.2 Pyroxene Results 43

6.3 Sources of Error 45

Chapter 7 Conclusions **47**

7.1 Future Work 48

Appendix:

Appendix A g-factor Calculation **51**

Bibliography **53**

List of Tables

4.1 Non-explored plume parameters for our present grain model. Nominal-case values from Heldmann et al. [1]. 15

5.1 Parameters to constrain 24
5.2 Shape-Defining Parameter Values 25

6.1 Characteristics of the curves that best fit the band-strength data. Grains heating model utilizing olivine as the dirt material. 36
6.2 Characteristics of the curves that best fit the band-strength data. Grains heating model utilizing pyroxene as the dirt material 45

List of Figures

3.1 Hydroxyl band strength data (309 nm wavelength band) as observed by LCROSS' UV-visible spectrometer. Data after 200 s post impact were ignored in the analysis presented herein. 8

4.1 Grain model schematic showing photodissociation of water vapor and direct photodissociation of ice. The parameters of this model are the mass of H_2O lofted by the plume ($M_{H_2O,grains}$), the volume fraction of dirt-inclusions in the ice-containing grains (f_v), and the ratio of ice-photodissociation probability to vapor photodissociation probability (α). 13

4.2 Sweating crater model schematic. Water sublimates from the hot impact-crater generating a H_2O cloud subject to photodissociation. The parameters of the sweating crater model are the total amount of H_2O sublimated ($M_{H_2O,sweat}$), the temperature of the released H_2O particles ($T_{H_2O,sweat}$), and the post-impact time at which water begins to be released(t_{delay}). 17

4.3 Prompt OH model schematic. OH radicals weakly bonded into the crater's surface regolith grains get expelled by Centaur's impact. The parameters of the model are the total amount of OH lofted ($M_{OH,prompt}$), and the temperature at which OH particles are released ($T_{OH,prompt}$). 19

5.1 Fitting method flow chart. $Result1$ is the set of values $SSWR$, C_1,C_2, and C_3 that minimizes $SSWR_{ijk}$ for a given set of altered OH data. $Result2$ is the set $Result1$ containing the minimum $SSWR$ among all combinations of curves. 31

5.2 $Result2$ of the fitting process. Least-squares minimization fitting all combinations of curves and selecting the combination (and respective weights) with least $SSWR^*$. The selected curves composing n_{total} determine the shape-defining parameter values of the fit, and the weighting coefficients of the minimization process define the size-defining parameters values. 32

5.3 Examples of data alterations used in the process of estimating confidence intervals in the results. Each original data point is randomly varied (three times in this example) with a normal distribution within its error bars. 32

6.1 The black squares represent the LCROSS OH data considered for the analysis. The thin lines on the background (single fits) are all of $[Results2]_l$. OH_{mean} is the average of the single fits. OH_{LCROSS} is the result of the LCROSS simulation with Table 6.1 values as inputs. 37

6.2 OH band strength data fitted with grains model only. Ignoring the prompt OH and sweating crater models in the fitting process distinctly shows the rise of at least two families of solutions. 39

6.3 Histograms of grain model parameter results. Results cluster around different values rather than spreading out around a single value. . . . 40
6.4 Histograms of prompt OH model parameter results. Distribution of results show an approximately normal distribution which results in the best constrained model. 41
6.5 Histograms of sweating crater parameter results. The distribution of total amount of water shows leans towards relatively low values. The sweating crater contribution to the simulated OH band strength is altogether relatively weak. 41

Chapter 1

Introduction

The Lunar CRater Observing and Sensing Satellite (LCROSS) mission was devised by NASA in order to confirm and characterize the presence of water-ice in permanently shadowed craters of the Earth's Moon. The LCROSS mission successfully proved the presence of water-ice at the Moon's poles [2]. Nevertheless, several questions about the characteristics of water in these shadowed areas are still open. One of the big motivations to confirm the presence of water is the possibility to utilize it for future exploring or colonizing-missions. Therefore, confirming the presence of water in the Moon is not only a question of *yes* or *no*. It is also relevant to know the amount of water present and characterize its conditions as much as possible. Previous work in our group used LCROSS data to learn about the observations taken during the mission [1, 2]. This work focuses on learning more about the conditions of the Moon's shadowed craters by studying a set of data not considered in detail before —the hydroxyl band strength data.

The LCROSS mission contained a total of nine scientific instruments. The hydroxyl band strength data were obtained from the processing of spectral measurements from the UV-visible spectrometer (VSP). Each set of LCROSS measurements contributes differently to what we can learn from the mission as a whole. Previous

studies already used LCROSS observational data to constrain the physical parameters of the impact-plume [2, 1]. The hydroxyl band strength may help characterize physical mechanisms that were not considered in previous studies. The three OH-producing processes herein hypothesized to contribute to the LCROSS observations are: the photodissociation of water from ice-containing grains in the impact-plume, photodissociation of water sublimated from the crater's surface, and the presence of OH radicals in the surface regolith that got ejected by LCROSS first impact.

We will review the LCROSS mission and the measurements relevant for this work. Then we will describe the general computer code used to simulate the LCROSS observations, including the OH producing mechanisms and their physical justification. The most extensive part of this project was developing the fitting method to constrain the parameters of the physical models, and estimating the confidence intervals in our results. This optimization process is more general than simulating the relevant and specific physical processes for the LCROSS mission; that process may be used to study other computational models with unknown parameters. Finally, we will conclude with a discussion of the results and our conclusions.

The basic methodology of the project is to simulate the physics of the LCROSS primary impact and the trajectory of the following spacecraft taking measurements in order to model the observational data. Using this computational simulation, we explored the input-parameter space of our physical models and fitted the computational results to the observational data. The fitting process systematically re-scales and changes physical model parameter values in order to minimize the difference between the computational and the observational results. We also make use of uncertainty in the OH LCROSS observational data to estimate the confidence intervals in our results.

A goal of this study is to learn about the Moon's permanently shadowed crater conditions by constraining the physical parameter values of our numerical

models. However, the fitting method resulted in multiple possible solutions. Some of the proposed models were only moderately constrained, and had relatively large confidence intervals.

Chapter 2

LCROSS Mission Overview

In 1998, measurements of neutron flux suggested the presence of hydrogen in the permanently shadowed craters located near the Moon's poles [3]. The observed neutron emissions are a signature of hydrogen rich environments, which could be in the form of water ice [4]. The publication of these observations by Feldman et al. was accompanied by estimates of buried water-ice. However, Feldman et al. acknowledged that their models may not be unique, and also mentioned inconsistencies between levels of neutron signatures and how they relate to the extend of shaded area [3]. The apparent detection of water in the cold traps was therefore not conclusive, which motivated the Lunar CRater Observing and Sensing Satellite (LCROSS) mission.

The main objective of the LCROSS mission was to confirm the presence or absence of water-ice in the lunar-polar cold traps. The four scientific goals of LCROSS were [5]:

1. Confirm the presence or absence of water ice in a permanently shadowed region on the Moon;

2. Identify the form/state of hydrogen observed at the lunar pole;

3. Quantify, if present, the amount of water in the lunar regolith with respect to hydrogen concentrations;

4. Characterize the lunar regolith within a permanently shadowed crater on the Moon.

The presented work will help achieve Goals 2, 3, and 4 by identifying molecules (H_2O and OH) present in the Moon's poles, quantifying the amount of water released from Cabeus crater by the LCROSS primary impact, and characterizing the composition of grains containing water-ice.

LCROSS was an "opportunity" mission launched with the Lunar Reconnaissance Orbiter. The LCROSS mission (performed in October 9, 2009) consisted of two spacecraft crashing into the Moon's Cabeus crater. The first impactor was an Atlas V upper-stage Centaur rocket (Centaur spacecraft) whose only goal was to blast shaded-surface material into sunlight. The second spacecraft (the *shepherding spacecraft* or just *SSC*) contained the LCROSS instrumentation and performed many of the mission's measurements. The SSC followed Centaur's trajectory with a $\sim$4 minute lag. The SSC successfully observed and transmitted observations of Centaur's impact-plume until it too finally crashed. The LCROSS instrumentation included a photometer, different types of cameras, different types of spectrometers, and other instruments. The particular set of data we will focus on is the hydroxyl (OH) band strength data measured from the SSC by the nadir-pointing UV-visible spectrometer (VSP).

Chapter 3

Hydroxyl Band Strength Data

The instruments in the LCROSS mission were devised to measure different characteristics of Centaur's impact-plume. Several sets of data have already been used to gain insight about the ejecta and plume evolution of the LCROSS mission. For example, the near-infrared (NIR) spectrometer data were used to estimate abundance of water and other volatiles [2], and the total light curve and color ratio from the VSP were used to constrain the morphology and evolution of the plume [1]. However, the OH band strength signal from the VSP has not yet been exploited for similar analysis.

The hydroxyl band strength data was filtered from the whole spectra measurements of the VSP. The VSP had a one-degree field of view (FOV) and a spectral range of 263-650 nm. The instrument was kept pointed towards Centaur's impact location (i.e. observing the impact-plume) as the SSC descended towards its own crash. Data were collected for 250 seconds — from the time Centaur impacted until the SSC lost signal. Further specifications of the VSP instrument and how it was used in for the LCROSS mission are detailed in [5]

The process of extracting the data was performed by collaborator Dr. Anthony Collaprete. The first step to retrieve the OH band strength from the VSP

spectrum was to apply a moving-average forward in time to increase signal-to-noise ratio. OH in sunlight emits in the 309 nm wavelength-band due to excitation from photodissociation or through fluorescent scattering [6]. Therefore, the OH band strength was then filtered out of the whole VSP data set by integrating the spectrum across two pixels (centered at 309.57 nm and 309.97 nm) and subtracting the continuum background signal (integrated from surrounding spectral regions of 306.81-308.39 nm and 311.54-313.51 nm).

The results of extracting the OH signal from the whole spectral range are presented in Fig. 3.1. The error bars represent two standard deviations of the moving average. The VSP perceived a rise in the OH band within the first $\sim$6 s after Centaur's impact. Around twenty seconds post-impact, the signal strength declined, only to rise up again to its maximum value at $\sim$35 s. Finally the band shows a continuous decrease in strength until nearly the end of the observation. We note that toward the end of the data collection period, the band signal rose again. However, it is not clear why this occurred, and might have been an instrumental issue occurring towards the end of the descent. Considering expert advice from LCROSS instrument scientist and the provider of the data, Dr. Anthony Colaprete, we decided to ignore data after 200 seconds post-impact.

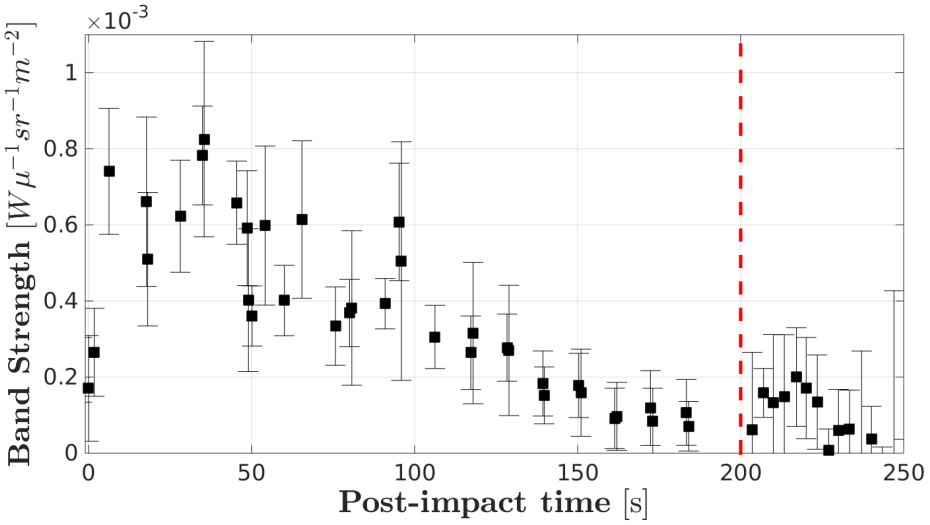

Figure 3.1: Hydroxyl band strength data (309 nm wavelength band) as observed by LCROSS' UV-visible spectrometer. Data after 200 s post impact were ignored in the analysis presented herein.

Chapter 4

Simulation Code

This work is a continuation of previous LCROSS studies already mentioned in Chapter 3, where a computational simulation was used to constrain plume parameter values and characterize the evolution of the plume (Heldmann et al. [1]). This work therefore uses many of the methods described by Heldmann et al. A comprehensive description of their model can be found in their paper (2015). We will restrict ourselves to a short description of Heldmann et al.'s base code, and a more detailed explanation of the improvements and new features added to their simulations for our purposes.

4.1 LCROSS simulation and improvements

The LCROSS simulation is a Monte Carlo computation that simulates a large number of real particles of regolith dust, ice grains, H_2O, and OH molecules through a scaled-down number of representative particles. Because of the rarefied conditions of the Moon, particles in the simulation are assumed to not collide with each other. The computational model simulates Centaur's impact-plume and the SSC trajectory throughout its descent. The plume is simulated as a disk of material lofted by Cen-

taur's impact. This impact-plume has two components, a sharp central spike and an inverted lamp-shade debris composed surrounding plume. Grains forming the overall plume are generated with a log normal size distribution with mean grain radius of $\mathcal{O}(1\mu\text{m})$ and a standard deviation of 0.7 the mean radius. The grain ejection speed is calculated as a function of grain distance from the material-disk center. Finally, the ejection angle of the grains is randomized within two angle ranges depending on which component of the plume they belong to.

In collaboration with other graduate students at The University of Texas at Austin, Yasvanth Poondla and Aayush Agrawal, we improved Heldmann et al.'s photodissociation model, the grain heating model, and added OH-producing mechanisms not considered before. Yasvanth Poondla developed the photodissociation and grain heating model, as well as the prompt OH mechanism. Aayush Agrawal developed the direct ice-photodissociation model. Yasvanth Poondla and Aayush Agrawal's physical models were integrated in this work in order to represent the OH data. Their mechanisms are an essential part of this work — the production of OH molecules in the simulation — and will be explained next.

4.1.1 Photodissociation model

Relevant to the work presented here is the photodissociation model for water molecules to produce OH radicals. The improvements on the photodissociation model were done by Yasvanth Poondla. Heldmann et al.'s photodissociation model was a probability check on all H_2O molecules in sunlight in order to generate a dissociation probability at 1 AU of 8.54×10^{-6} s^{-1} based on Huebner and Mukherjee photodissociation rates [7]. The resulting OH particle was assumed to have the same velocity as the original H_2O particle. As an improvement to this photodissociation model, we considered the effect of how the excess photon energy is distributed after a dissociation event. In the process of accounting for the excess photon energy, each

photodissociation event is treated as a hard sphere collision between the incoming photon and the H_2O molecule. If the dissociation event occurs (based on a random-number draw) isotropic scattering about the center of mass is assumed. Finally, we calculate how the excess energy is redistributed among the recoil velocities based on the work of Wu and Chen [8], who calculated the velocity distributions of hydrogen and hydroxyl after solar photodissociation of water. This improvement to the dissociation model better represents how water dissociates in sunlight. The net result was faster moving OH particles, which produce an OH cloud about 30% larger than the previous simpler model. This photodissociation model is used for some of our OH-producing mechanisms explained below.

4.1.2 Grain heating model

Besides improving the photodissociation model, our work also improved Heldmann et al.'s grain heating model. Previous simulations considered two scenarios of how water lofted into sunlight absorbed energy. The previous options of ice-containing grains had either pure-dirt or pure-aggregate-snow optical properties. The first scenario had dirt grains surrounded by an optically-thin layer of ice. This model yielded dark (low albedo) grains that warmed quickly in sunlight and rapidly sublimed off their water-ice layers. The second scenario had the impact-plume consisting of two kinds of grains: pure ice and pure dirt. In this case, the ice grains had a very high albedo and did not sublime rapidly.

We considered the intermediate scenario, where ice-containing grains and their properties are a combination of ice and dirt. The heating model was mostly developed by Yasvanth Poondla. We calculated albedo and other optical properties of small spherical particles using Mie Scattering theory, explained in detail by Wiscombe [9]. We also utilized the Maxwell-Garnet mixing rule to calculate the properties of combined materials, in our case, water and dirt consisting of either

olivine or pyroxene, both common lunar regolith materials [10, 11]. Using these theories, we calculated the optical and thermal properties for different volume fractions of dirt-inclusions, e.g. 10% olivine, 20% pyroxene, and so forth.

The key assumptions of our revised grain heating model are that: (1) dirt in ice-containing grains is homogeneously distributed; (2) grains are perfect spheres. The outputs of the grains heating model are the albedo and emissivity of the grain particles. The improved grain heating model is significant for one of the OH-producing mechanisms, which are explained next.

4.2 OH producing mechanisms

4.2.1 Mechanism 1: OH from grains

The first OH-producing mechanism comes from the photodissociation of H_2O lofted by the impact-plume. This mechanism contributes to the OH band strength signal through two sub-mechanisms: photodissociation of vapor (as assumed by Heldmann et al.) and direct photodissociation of ice. The whole grain OH-producing mechanism is illustrated in Fig. 4.1.

Photodissociation of water vapor

We have already discussed how grains lofted by Centaur's impact are initialized in the simulation (Section 4.1). Once the grains reach sunlight, they absorb and emit energy through our grain heating model, and ice sublimates into water vapor molecules. When water reaches the vapor state, it is subject to photodissociation through our photodissociation model (Section 4.1.1). Finally, if photodissociation occurs, OH molecules are created. Those OH molecules that remain in sunlight and within the one-degree FOV of the VSP detector are counted towards the simulated OH signal.

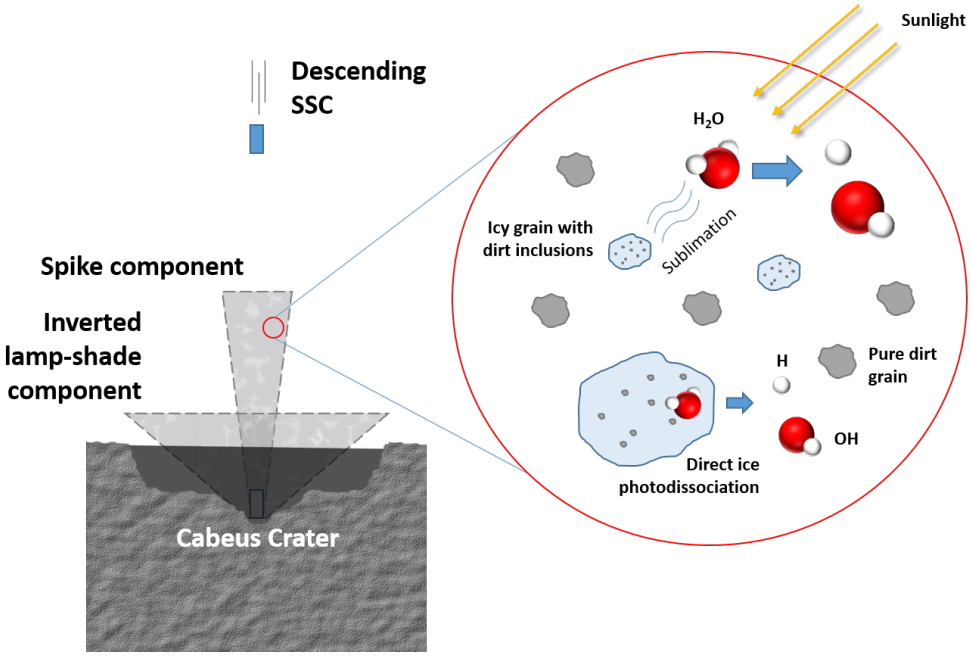

Figure 4.1: Grain model schematic showing photodissociation of water vapor and direct photodissociation of ice. The parameters of this model are the mass of H_2O lofted by the plume ($M_{H_2O,grains}$), the volume fraction of dirt-inclusions in the ice-containing grains (f_v), and the ratio of ice-photodissociation probability to vapor photodissociation probability (α).

Photodissociation of ice

Besides photodissociation of water vapor, we also analyzed the possibility of direct photodissociation of water-ice in the grains. The direct ice photodissociation model was developed by Aayush Agrawal. Photodissociation of ice is significantly different from photodissociation of vapor for several reasons. One reason is that once an H_2O molecule dissociates within ice, the end products still have to escape from the binding energy of the grain as a whole. The resulting photodissociation products have to diffuse out of the grain, but may in the process recombine with other particles instead.

There are methods to estimate the direct photodissociation of bulk ice by

calculating or measuring the yield products of ice being irradiated (e.g. Quickenden et al. [12] and Gerakines et al. [13]). However, in our case we also need to estimate the fraction of UV energy that is absorbed by water molecules from total absorbed energy of a micron-sized grain. It was not obvious how to do this. This process would be better measured experimentally and such measurements could not be found. Instead, we used a simple model to characterize photodissociation of ice. We assumed that the probability of OH production by direct ice-photodissociation is a fraction of the probability for water-vapor molecules to photodissociate:

$$P_{ice} = \alpha P_{vap} \tag{4.1}$$

The term α is the ratio of ice-photodissociation probability to vapor-photodissociation probability, presumed to be between zero and one. This quantity will be a parameter to be determined by fitting to the LCROSS measurements, and will be explained in more detail later in Section 4.2.1.

There is a significant difference relevant to our studies between the production of OH coming either from water vapor or ice, namely the resulting speed of the OH particles. OH particles from vapor dissociation have a recoil speed of the order of $\sim$ 1 km/s. On the other hand, the speeds of OH particles from direct ice photodissociation are presumed to be the thermal speeds based on the original grain's temperature ($\sim$ 300 m/s). Therefore, the slower OH originating from ice may remain inside the FOV longer than OH particles originating from water vapor. This characteristic will be important once we start considering how to replicate the OH band strength data. Therefore, we are not just interested in the amount of OH produced by photodissociation of H_2O, but also the source (either H_2O vapor or solid ice) of the produced OH.

Parameters describing the grains model

There are many parameters associated with the grain model. However, many of these parameters were already constrained by Heldmann et al. [1].Therefore, we kept Heldmann et al.'s nominal-case parameter values (summarized in Table 4.1) constant in our simulations, and focused on a total of three parameters for the grains model that we aim to fit. These parameters are the total mass of water lofted by the plume (M_{H20}), and the parameters f_v and α introduced by our improvements to the simulation.

Table 4.1: Non-explored plume parameters for our present grain model. Nominal-case values from Heldmann et al. [1].

Parameter	**Nominal Value**
Spike mass fraction	20%
Cone grain mean radius	1.6μm
Cone angle	67^o
Cone grain velocity limit	800 m/s
Spike grain mean radius	3.5 μm
Spike angle	12^o
Spike grain velocity limit	1000 m/s

The first unknown parameter is the total amount of water lofted in the impact-plume. This parameter is obviously related to the amount of OH produced from vapor: more water lofted into sunlight results in more water available to photodissociate either directly from ice or from sublimated vapor.

The second parameter is the volume fraction of dirt inclusions in the ice-containing grains (f_v). This parameter was already introduced in Section 4.1.2 where we described the heating model. The f_v parameter affects the production of OH because grains with higher f_v (i.e. more dirt) absorb more energy and heat up faster. Larger f_v values sublimate ice faster and therefore there is less water-ice and more water-vapor available for photodissociation in the plume compared to lower values of f_v. We assumed f_v remains constant as water sublimates from the grains.

Therefore, as water sublimates, grains also lose dirt mass so that the f_v remains the same.

Finally, the third parameter, α, is the ratio of ice-photodissociation probability to vapor-photodissociation probability (see Eq. (4.1)). This parameter comes from our assumed ice-photodissociation model. The purpose of α is to account for the effects of potential OH recombination within the ice-crystal, diffusion through the crystal, overcoming the grain binding energy, etc. This value could potentially be a function of other grain properties such as grain-size, the type of dirt material, f_v, etc. Future laboratory work could explore the properties of α and determine its dependencies. For now, we assumed α to be a constant value to be fitted in our simulation.

To summarize the assumptions of the grain model, in addition to assumptions (1) and (2) for the grain heating model mentioned in Section 4.1.2 we assumed: (3) grain volume fraction of olivine or pyroxene inclusions remains constant; therefore, as water sublimates from a grain, the grain loses dirt such that f_v remains the same. (4) grains contain only two materials — ice and dirt.

4.2.2 Mechanism 2: Sweating crater model for H_2O vapor production

The sweating crater model is a continuous source of water vapor emanating from the immediate vicinity of Centaur's impact location. Once the water vapor reaches sunlight, it is able to photodissociate. The reasoning behind the model is that the high energy impact — a 2366 kg spacecraft crashing at $\sim$2.5 km/s — generated a hot region at the impact-location that may have gradually sublimated remaining surface-water. Indeed, the Lunar Reconnaissance Orbiter Diviner Instrument measured a hot ($\sim$1,000 K) crater created by Centaur's impact [14]. An illustration of the model is shown in Fig. 4.2.

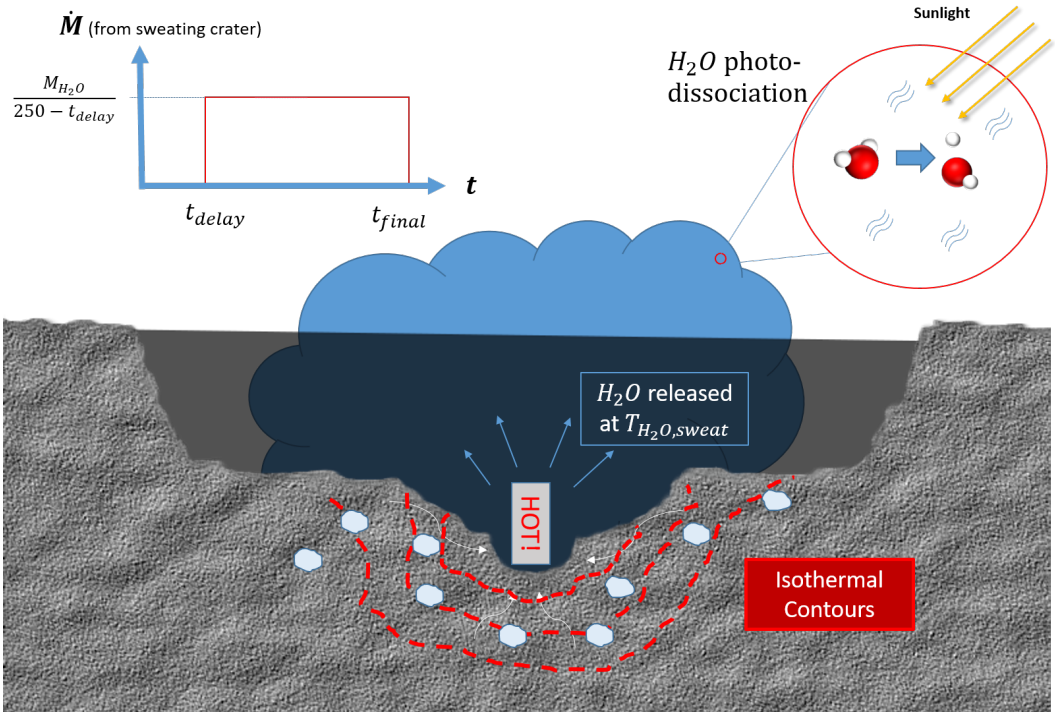

Figure 4.2: Sweating crater model schematic. Water sublimates from the hot impact-crater generating a H_2O cloud subject to photodissociation. The parameters of the sweating crater model are the total amount of H_2O sublimated ($M_{H_2O,sweat}$), the temperature of the released H_2O particles ($T_{H_2O,sweat}$), and the post-impact time at which water begins to be released(t_{delay}).

Parameters describing the sweating crater model

We use three physical parameters to describe the SC model. The first parameter is the total amount (in kilograms) of water sublimated by the hot crater ($M_{H_2O,sweat}$). We assume that the water is released at a constant rate. The sweating crater model is essentially a cloud of water expanding from the impact location. Larger rates of water released generate a denser H_2O cloud, which in turn produces larger amounts of OH.

The second parameter is the temperature at which water molecules are being released ($T_{H_2O,sweat}$). Water molecules are released in a uniformly-random direction

with a thermal speed based on a Maxwell-Boltzmann probability distribution:

$$f(v) = 4\pi v^2 \Big(\frac{m}{2\pi k_B T}\Big)^{3/2} e^{\left(\frac{-mv^2}{2k_B T}\right)} \tag{4.2}$$

where k_B is Boltzmann's constant, m is the mass of the gas molecule, T is the mean temperature of the surface (and the gas), and v is the molecules' speed. The temperature at which these particles are released affects how fast they reach sunlight and the amount of time they remain inside the FOV.

The last parameter in this model is an arbitrary time delay (t_{delay}). The time delay sets the post-impact time at which the sweating crater model begins releasing water. We assumed the water was released at a steady rate equal to $M_{H_2O,sweat}/(t_{final} - t_{delay})$. The goal of utilizing this parameter is to account for the time it took the ice not lofted by the impact to heat up, vaporize, and percolate from beneath the ground. The time delay obviously has a direct impact on the time-evolution of the sweating crater.

4.2.3 Mechanism 3: Prompt OH directly evolving from the crater

The prompt OH model is based on data suggesting the presence of OH particles in the permanently shadowed craters on the Moon [15]. We assumed these OH radicals were weakly adsorbed and trapped in the surface regolith. The presumed mechanism of release is from the grinding and shearing of the shocked deformed regolith, a process occurring very rapidly (< 1 s). Once the Centaur spacecraft impacted the Moon, these OH particles were ejected along with the plume material and at a characteristic thermal velocity. While in the two previously described mechanisms H_2O first has to dissociate to produce OH, this prompt mechanism is instantaneous because the OH particles are already present. The prompt OH model therefore generates a simulated OH signal at early times in the simulation. However, the prompt OH contribution to the simulated OH band strength signal quickly dies

off since the model does not continuously generate OH particles. The prompt OH model is illustrated in Fig. 4.3.

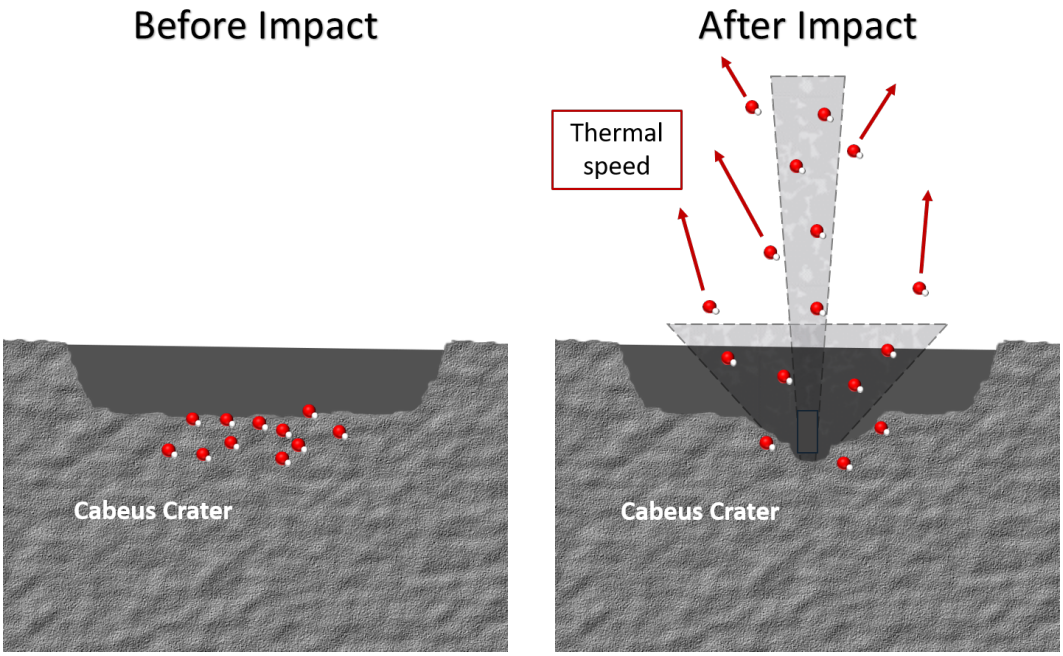

Figure 4.3: Prompt OH model schematic. OH radicals weakly bonded into the crater's surface regolith grains get expelled by Centaur's impact. The parameters of the model are the total amount of OH lofted ($M_{OH,prompt}$), and the temperature at which OH particles are released ($T_{OH,prompt}$).

Parameters describing the prompt OH model

This model has only two parameters associated with it. The first parameter is the amount of OH mass lofted by Centaur's crash. This defines the strength of the prompt OH contribution to the OH band strength data. The second parameter is the characteristic temperature at which the grains are released. Just as for the sweating crater model, the temperature parameter affects the OH thermal speed, which in turn affects for how long the particles remain inside the VSP instrument's FOV.

Chapter 5

Fitting Method

There is a total of 8 parameters to be constrained in the OH-producing models described in Chapter 4. The values for these 8 parameters will be chosen by comparing the simulation results to the experimental observations of the actual LCROSS mission. The goal is to explore the parameter space of the simulation to find the values that *best* represent the observations. However, running the LCROSS simulation in order to explore the whole parameter space is not feasible.

As mentioned before, the LCROSS simulation is a Monte Carlo calculation with representative particles. A larger number of particles in the simulation make for a better representation of the system. However, we are interested in the OH particles in particular, which are just a fraction of the original number of particles for a given simulation because OH particles mostly originate from the dissociation of H_2O. Furthermore, out of this relatively small number of OH-particles, our results only account for particles inside the instrument's small (1^o cone) field of view. This reduces the number of observed OH particles even further. For these reasons, the cost of our simulations is more expensive than previous simulations which concentrated on more plentiful H_2O molecules or dust grains. Because exploring the whole parameter space is not feasible, we developed a fitting method to find the *best*

parameter values for our simulations and quantify the confidence in our results.

One thing not mentioned so far is how we compare the LCROSS-observed OH band strength to our computational result, which are in terms of sun illuminated OH particles *in-view*. This is done by estimating the OH band-strength emission from the column density of illuminated OH molecules *in-view*. The process involves an emission rate factor, also known as Chamberlain g-factor, or just g-factor [16]. Details of how this calculation is performed are discussed in Appendix A. Once we combine the three models' contributions and estimate the observed band strength, we can directly compare the computational results with the experimental observations in the actual fitting process.

The fitting process is divided into two parts. Part I is the general process of exploring the parameter space and fitting the eight model parameters to *a* particular set of OH data. Part II aims to quantify the confidence of our data fit. Part II systematically repeats the procedures of Part I multiple times in order to account for the measured uncertainty in the LCROSS OH band strength observations. The process of Part II provide error bars on our eight fitted parameters describing the physics of the OH production.

5.1 Part I: Fitting the Hydroxyl Band Strength

5.1.1 Categorization of parameters

From the explanation of the models in Section 4.2, the parameters to be fitted to the OH band strength are: for the grains model, the mass of H_2O lofted along with the grains ($M_{H_2O,grains}$), the volume fraction of inclusions in the water-containing grains (f_v), and the ratio of direct ice-photodissociation to vapor-photodissociation (α); for the prompt release OH model, we have the amount of OH directly lofted by Centaur's impact ($M_{OH,prompt}$), and the characteristic OH particle temperature

($T_{OH,prompt}$); and for the sweating crater model, the total amount of H_2O sublimated from the hot crater throughout the simulation ($M_{H_2O,sweat}$), the temperature at which water particles were being released ($T_{H_2O,sweat}$), and the time (relative to impact) at which the sublimation of water initiated (t_{sweat}). Given the physical significance of these parameters, and the effect they have on the simulation, these parameters were divided into two sub-groups: size-defining parameters and shape-defining parameters.

- **Size-defining parameters**: set the amplitude of the simulated observation.
    1. Mass of H_2O lofted along with the grains, $M_{H_2O,grains}$ (Grains Model);
    2. Mass of H_2O sublimated from the hot crater, $M_{H_2O,sweat}$ (Sweating Crater Model);
    3. Mass of OH lofted from impact, $M_{OH,prompt}$ (Prompt OH Model).
- **Shape-defining parameters**: determine the curve-shape of the simulated observation.
    1. Ratio of direct ice-photodissociation to vapor-photodissociation, α (Grains Model);
    2. The volume fraction of inclusions in the water-containing grains, f_v (Grains Model);
    3. The temperature at which water particles were being released, $T_{H_2O,sweat}$ (Sweating Crater Model);
    4. The time (relative to impact) at which the sublimation of water initiates, t_{sweat} (Sweating Crater Model);
    5. The characteristic OH particle temperature, $T_{OH,prompt}$ (Prompt OH Model).

The size-defining parameters are all the mass parameters from the three models. Because of the way the simulation works, changing the value of these parameters do not affect the temporal evolution of the representative particles. These size-defining parameter only change the ratio of real-gas to computational particles (i.e. f_{num}). Graphically—a big part of our analysis relies on graphic representations—changing these parameters scales the curves of simulated OH in view, but does not otherwise affect the time dependence of the curves. Physically, changing these parameters increases or decreases the substance-amount homogeneously in space and time, but the time-dependence of the simulated observation is not changed.

The shape-defining parameters on the other hand do affect the temporal evolution of the particles, and thus, change the time dependence of the simulation. For example, increasing f_v causes grains to heat up faster, which in turn causes faster sublimation, and thus faster vapor photo-dissociation. Therefore, for higher values of f_v, the simulated observation shows more OH particles from grains-sublimated vapor at earlier times. Adjusting these shape-defining parameters alters the shape of the OH curves.

The differences between the effects of the shape-defining and size-defining parameters affect how we treat them in the fitting process. Table 5.1 shows a summary of the eight parameter-values to be found. Because of how they affect the time evolution of the results, analyzing the shape-defining parameters is more involved. We treated these parameters by discretizing their parameter space.

5.1.2 Discretization of the Parameter Space

As mentioned before, it is not feasible to run the entire Monte Carlo LCROSS simulation repeatedly in order to fit the OH band strength data by exploring the whole parameter space. Each full Monte Carlo plume simulation consumes ∼25 CPU hours to obtain a smooth result without stochastic fluctuations. If we want

Table 5.1: Parameters to constrain

Model	**Size-defining parameters**	**Shaped-defining parameters**
Grains	$M_{H_2O,grains}$ (kg)	α (*non-dimensional*)
		f_v (*non-dimensional*)
Sweating Crater	$M_{H_2O,sweat}$ (kg)	t_{sweat} (s)
		$T_{H_2O,sweat}$ (K)
Prompt OH	$M_{OH,prompt}$ (kg)	$T_{OH,prompt}$ (K)

to explore 10 different values for the eight available parameters, the computations will cost about 25×10^8 CPU hours. Therefore we discretized the parameter sub-space of the shape-defining parameters. This was done by computing the curves of OH in view for discrete sets of values for each shape-defining parameter (see Table 5.2 for range of parameter-values explored) and then interpolating between the pre-computed curves. These pre-computed curves and interpolations between the pre-computed curves were saved into a repository of curves, to which we will refer as the *curves bank*. This curves bank contains curves of each model, with different combinations of shape-defining parameter values. Examples of three curves found in the curves bank are:

`Grains (`f_v`:30% , `α`:0.1)`

`Sweating Crater (`T_{H_2O}`:500 K , `t_d`:40 s)`

`Prompt OH (`T_{OH}`:1200 K)`

The curves bank will be used to access the parameter values in a systematic way as we loop through all the possible combinations of parameter values. This will be explained with more detail later in Section 5.1.5.

For the size-defining parameter values, we could similarly discretize the parameter sub-space using pre-computed curves for the curves bank. However, because of the nature of the size-defining parameters (explained in Section 5.1.1), changing

their value only scales the curves up and down proportionally. That is, for given values of shape-defining parameters in any of the three models, we can represent the whole mass-parameter space with an arbitrary scaling coefficient. Hence, we decided to represent the size-defining parameters with scaling coefficients, rather than with pre-computed curves in the curves bank. This allows us to have a continuous representation of the size-defining parameter sub-space while keeping the size of the curves bank smaller — something that is computationally desirable in the fitting method.

Table 5.2: Shape-Defining Parameter Values

Model	**Parameter**	**Range of values**
Grains	α	$0.01 - 0.8$
	Dirt Volume Fraction (f_v)	$0\% - 80\%$
Sweating Crater	Time Delay (t_d)	0 - 160 s
	H_2O Temperature	20 - 2200 K
Prompt OH	OH Temperature	100 - 1700 K

5.1.3 Combining OH-Producing Mechanisms to Estimate Hydroxyl Band Strength Observations From Computational Results

Up until now, we have considered the OH producing models individually and independently of each other. However, if these physical mechanisms were indeed present in the LCROSS mission, the LCROSS instrumentation would have observed these mechanisms simultaneously. Therefore, the three contributing models have to be considered together to be compared to the OH measurements.

For simplicity, consider a specific set of shape-defining parameter values. That is, consider a specific curve in the curves bank for each of our three physical models. We then have a total of 3 curves, one for the prompt OH model, one for the grains model, and one for the sweating crater model. These curves will be labeled n_{prompt}, n_{grains}, and n_{sweat} accordingly. Along with the scaling coefficients that

represent the size-defining parameters— let's call these C_1, C_2, and C_3— we can combine the three physical model contributions as follows:

$$n_{total,ijk} = C_1 n_{prompt,i} + C_2 n_{grains,j} + C_3 n_{sweating,k} \tag{5.1}$$

Here, $n_{total,ijk}$ is the combined OH contribution to the hydroxyl band strength. The subscript i in $n_{prompt,i}$ indicates we are using a specific curve i within the available prompt OH curves in the curves bank. Similarly, indices j and k represent specific curves for grains and sweating crater models.

5.1.4 Least-squares fit for a particular combination of curves

Most of the work for the fitting process described so far has been to set up the fitting computations. The next step in the fitting process is where we actually start comparing the computational results to the observational data. In this we make use of a least squares minimization. embodied in MATLAB's tool `lsqcurvefit` for the least-squares algorithm [17].

Still consider a specific combination of curves from the curves bank, namely $n_{total,ijk}$ from Eq. (5.1). We want a measure of how well $n_{total,ijk}$ represents the OH band strength measurements. In order to quantify this quality, we utilized the sum of squared *weighted* residuals (SSWR):

$$SSWR_{ijk} = \sum_{\zeta=1}^{N_{data}} [\frac{n_{exp,\zeta} - n_{total,ijk}(t_\zeta)}{\sigma_\zeta}]^2 \tag{5.2}$$

where N_{data} is the number of observational data points (35 data points), $n_{exp,\zeta}$ is a particular OH band strength measurement taken at time t_ζ with uncertainty σ_ζ. $n_{total,ijk}(t_\zeta)$ is simply the value of the computational simulation $n_{total,ijk}$ at the time $n_{exp,\zeta}$ was taken. This sum in Eq. (5.2) represents the aggregate difference between the band strength data points and the computational results. Lower values

of $SSWR_{ijk}$ mean that $n_{total,ijk}$ represents the observational data better. We divide, each difference between $n_{total,ijk}(t_\zeta)$ and $n_{exp,\zeta}$ by σ_ζ to give more importance to experimental measurements with less uncertainty. In other words, we weight the difference between a data point and the computational results by the inverse of that point's uncertainty. For example, a point with a difference Δ and small uncertainty σ_ζ will contribute more to $SSWR_{ijk}$ than a point with the same difference Δ and large uncertainty σ_ζ.

Notice that because $n_{total,ijk}$ is actually a function of the weighting coefficients C_1, C_2, and C_3, $SSWR_{ijk}$ is also a function of these same coefficients. Therefore, using a least squares fit, we can minimize $SSWR_{ijk}$ by changing the values C_1, C_2, and C_3. The result of the least squares fit is the set of weighting coefficients for $n_{prompt,i}$, $n_{grains,j}$, and $n_{sweat,k}$ that gives the minimum possible value of $SSWR_{ijk}$. This set of coefficient values will be denoted $C^*_{1,ijk}$, $C^*_{2,ijk}$, and $C^*_{3,ijk}$. The minimum sum of squared weighted residuals will be denoted as $SSWR^*_{ijk}$. Together $C^*_{1,ijk}$, $C^*_{2,ijk}$, $C^*_{3,ijk}$, and $SSWR^*_{ijk}$ as a group will be referred to as *Result 1.*

For a given set of shape-defining parameters — defined by the specific curves comprising $n_{total,ijk}$ — Result 1 is a fit of the hydroxyl band strength data. However, choosing a different combination of curves for $n_{total,ijk}$ may result in a better fit with a lower value of $SSWR_{ijk}$. Therefore, all combinations of curves have to be tested.

5.1.5 Testing all combinations of curves

Until now, we have considered an arbitrary combination of shape-defining parameter values. These values are implicitly denoted by indices i, j, k, which correspond respective parameter values of the comprising curves. However, nothing guarantees that our arbitrary choice is indeed the *best* choice of shape-defining parameters values. We will use the curves bank to find the *best* choice of shape-defining values.

The final step to find the whole set of parameters values is to loop through

the curves bank, test all combination of curves, and keep track of the lowest $SSWR$, also keeping track of its respective shape-defining and weighting-coefficients values. The procedure then is as follows:

1. Get a curve for each model from the curves bank; call it set ijk
2. Fit set ijk to LCROSS' OH data to find [Result 1]$_{ijk}$ and $SSWR^*_{ijk}$ using the least squares method in Section 5.1.4
3. Get a different combination of curves from the bank, call it set ijk'
4. Fit set ijk' to find [Result 1]$_{ijk'}$ and $SSWR^*_{ijk'}$.
5. Repeat until all combinations of curves have been tested
6. From among all the combinations of curves, find the combination with lowest value of $SSWR^*_{ijk}$ (this quantity will be named $SSWR^*_{min}$)

We thus find the *best* fit out of all the $SSWR^*$ values and corresponding parameter values — the fit with the minimum value of $SSWR^*$. We call [Result 1]$_{ijk}$ with the lowest value $SSWR^*$ $Result2$. $Result2$ is the completion of Part I of the fitting process, where we have successfully fitted a set of OH band strength data. Part I methodology can be observed visually in Fig. 5.1.

$$Result2 = min\ SSWR^*\ of\left\{ Result1]_{111}\ ,\ Result1]_{112}\ ,\ ...\ ,\ Result1\Big]_{ijk}\ ,\ ...\ \right\} \tag{5.3}$$

(for all combinations of curves ijk)

We will use $Result2$ for Part II of the fitting process, where we will find confidence intervals of our fit. In order to keep track of $Result2$ components, we will denote them as $SSWR^*_{min}$ and $n_{total,min}$. These are the minimum $SSWR^*$ among all $SSWR_{ijk}$ values and the corresponding n_{total}. The computational result

$n_{total,min}$ is composed of $n_{prompt,min}$, $n_{grains,min}$, and $n_{sweat,min}$ appropriately scaled by $C^*_{1,min}$, $C^*_{2,min}$, and $C^*_{3,min}$.

*Result*2 for the OH band strength data is shown in Fig. 5.2. This example however is NOT the final result of our fit to the data. This image is only for clarification purposes of the discussed methods so far. The figure shows the experimental data, the contributing OH producing models already scaled by $C^*_{1,min}$, $C^*_{2,min}$, and $C^*_{3,min}$, and the total simulated band strength $n_{total,min}$.

5.2 Part II: Confidence intervals on the fit

We want to estimate the uncertainty in the results of the best fit parameter values, namely *Result*2. In other words, we would like to find confidence intervals of *Result*2. To do so, we looked at how the uncertainty in the OH measurements can affect the value of these *best* parameters. Therefore, the confidence intervals of our fit will depend two things: how sensitive the computational results are to variation in values of the parameters, and the uncertainty in the OH data itself. Part II methods are developed from the methodologies described in Part I (Section 5.1) and are a continuation of Part I methods rather than an independent process.

The parameters in our models represent physical characteristics of the process they represent. Therefore, the best fit parameter values chosen for *Result*2 estimate the actual physical characteristics of the mission. However, the OH data collected during the LCROSS mission, as any type of measurement, has uncertainty to it. If the true OH signal was different from what was actually measured, the best parameter values might have been different.

We consider the possibility that the true band strength values lie within a normal distribution around the measured value. Therefore, we varied the experimental data to account for this possibility. Each experimental data point (n_ζ) was

altered as follows:

$$\tilde{n_\zeta} = n_\zeta + R_\zeta \sigma_\zeta \tag{5.4}$$

Where $\tilde{n_\zeta}$ is the altered band strength measurement; σ_ζ is the standard deviation of data point n_ζ (same value as in Eq. (5.2)); and R_ζ is a normally-distributed random number with a mean value of zero and variance of 1, but still limited to lie within $\pm\sigma$ of the measured value. Each data point n_ζ was given a different random number R_ζ, so the variation of a given data point was independent of all others. An example of three sets of altered data is shown in Fig. 5.3.

After altering the OH data, we repeated Part I of the fitting process, and looked at how $Result2$ changed. That is, we looked at how varying the data affected the results of best fit parameter values and repeated the process for multiple sets of altered OH data. Each set of results is named $[Result2]_l$, where the subscript l denotes a particular alteration to the OH data.

After altering and fitting the data for a sufficiently large number of times, we averaged the results and calculated the standard deviation for each parameter. The final results of parameter values are the average values from all of $[Results2]_l$. The confidence intervals of our results are the standard deviation of the parameter-values. The final result for $M_{H_2O,grains}$ looks as follows:

$$\Big[M_{H_2O,grains}\Big]_{best,final} = avg\Big\{[M_{H_2O,grains}]_l\Big\} \pm std\Big\{[M_{H_2O,grains}]_l\Big\} \tag{5.5}$$

And similarly for all other parameters. Fig. 5.1 shows the complete fitting procedure schematically.

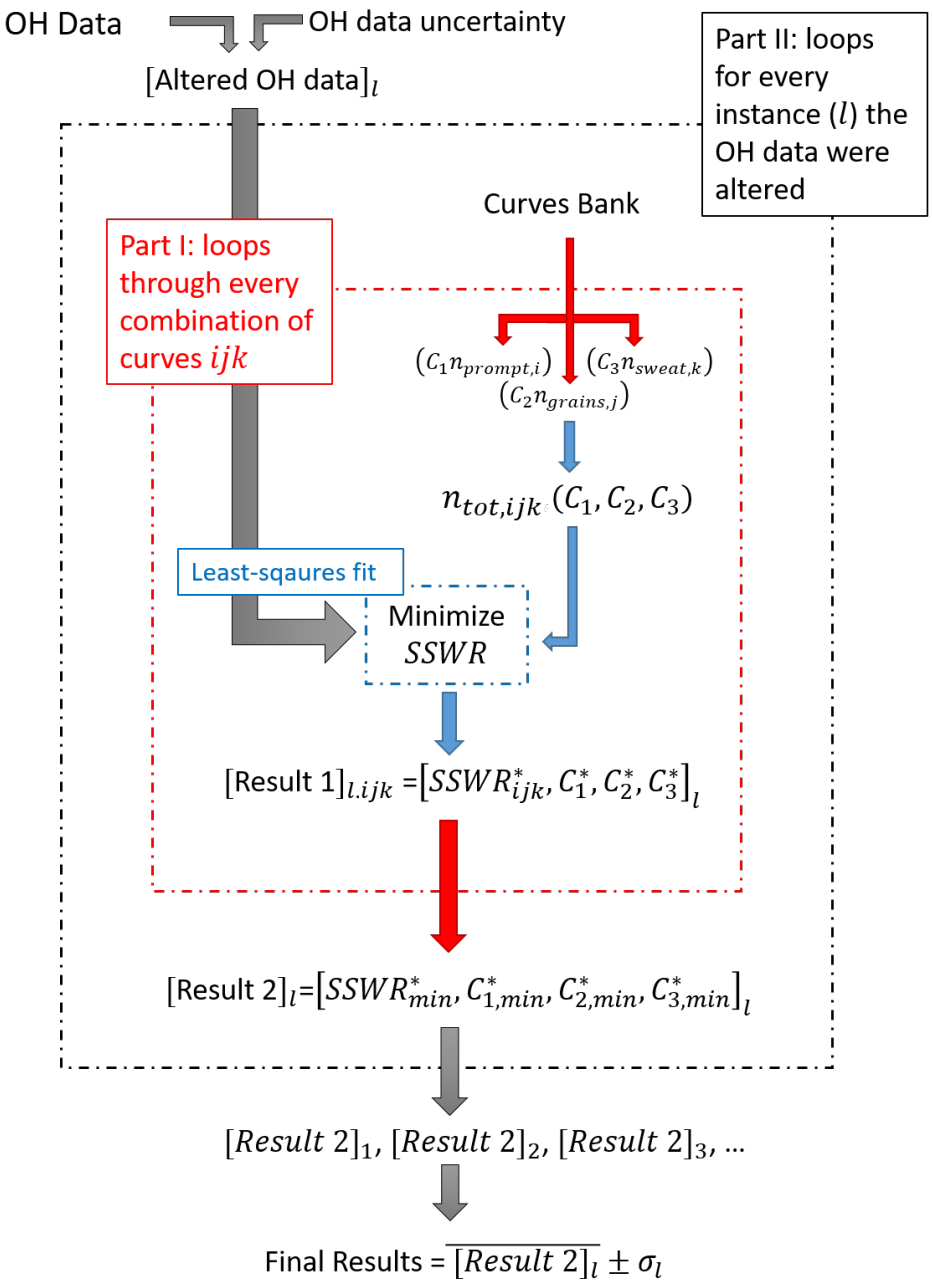

Figure 5.1: Fitting method flow chart. *Result*1 is the set of values $SSWR$, C_1,C_2, and C_3 that minimizes $SSWR_{ijk}$ for a given set of altered OH data. *Result*2 is the set *Result*1 containing the minimum $SSWR$ among all combinations of curves.

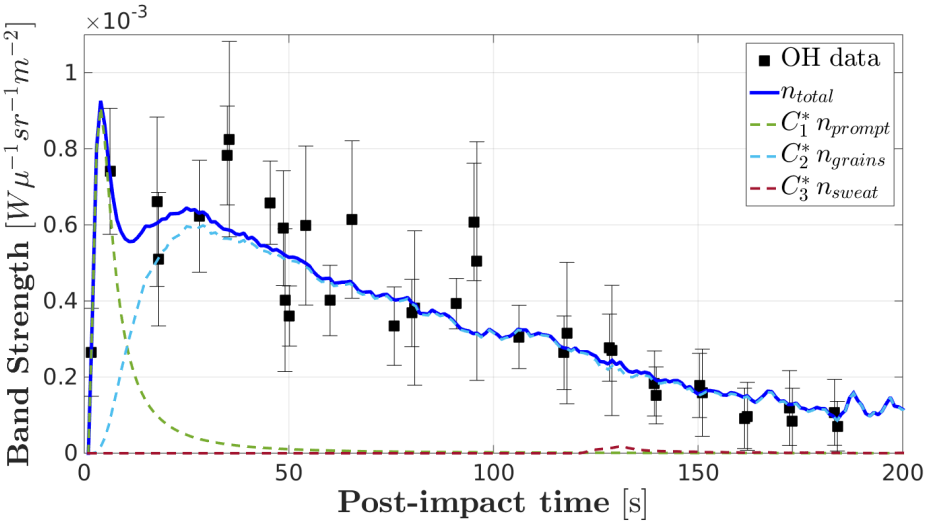

Figure 5.2: *Result*2 of the fitting process. Least-squares minimization fitting all combinations of curves and selecting the combination (and respective weights) with least $SSWR^*$. The selected curves composing n_{total} determine the shape-defining parameter values of the fit, and the weighting coefficients of the minimization process define the size-defining parameters values.

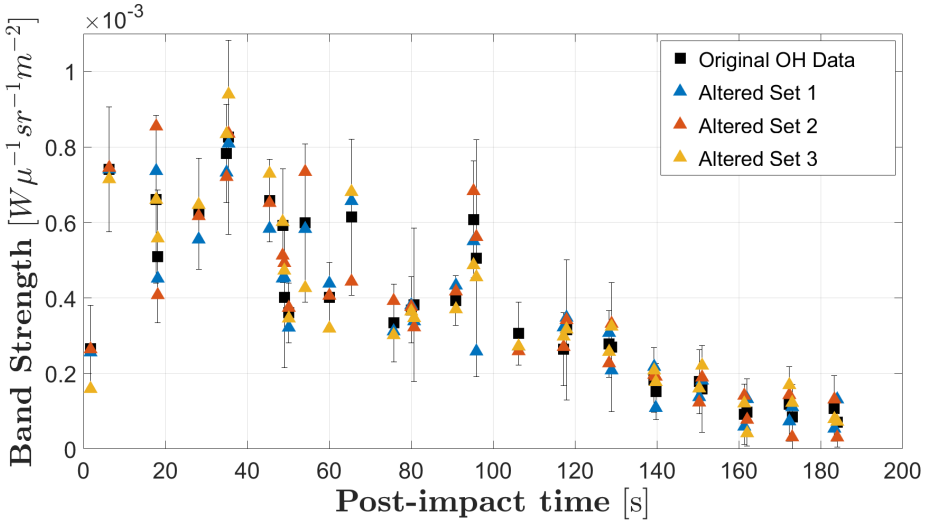

Figure 5.3: Examples of data alterations used in the process of estimating confidence intervals in the results. Each original data point is randomly varied (three times in this example) with a normal distribution within its error bars.

Chapter 6

Results and Discussion

6.1 Olivine Results

The final results for the parameter values and their uncertainties are presented in Table 6.1. The amount of water lofted amid the grains by Centaur's impact ($M_{H_2O,grains}$) was 800 ± 200kg. The result of f_v being $11 \pm 9\%$ means that water-containing grains were mostly water, but some dirt was necessary to darken them enough to sublimate water faster than if they were pure-ice grains. Finally for the grains, α is best fit as 0.11 ± 0.07 which means that a molecule of water still within water-ice has about a one-tenth probability to produce free OH from photodissociation compared to the probability of photodissociation of water-vapor.

Previous work by Colaprete et al. estimated a plume with total mass of 3150 kg with 5.6% being water, i.e. 180 kg of water in the plume [2]. First, they estimated the 3150 kg of ejecta mass by providing an approximate optical depth for the plume using the highest overall brightness observation in the VSP. Then, they utilized this optical depth to estimate a number density of particles. This data was then employed to obtain an estimated amount of total ejecta mass. For the estimate of water content in the plume, Colaprete et al. looked at the reflectance spectra

for the 1.87 μm band in the NIR spectrometer. Along with calculated absorption cross-sections from the high-resolution transmission molecular absorption database (HITRAN), Colaprete et al. estimated a column density of H_2O particles. As in the ejecta mass case, the H_2O column density was in turn used to estimate the total mass (water and ice) of H_2O. Our work however resulted in more than 4 times the amount of H_2O obtained by Colaprete et al.. It is not clear why Colaprete et al.'s and this work's results differ, but this is probably due to different assumptions from both studies (e.g. underlying assumptions in Colaprete et al.'s calculations, assumptions of g-factor calculations in our estimates of band strength, choices of material composing the impact-plume, etc.).

The amount of sublimated water from the hot "sweating" crater ($M_{H_2O,sweat}$) was fit to be 300 ± 300 kg released at a temperature of 1800 ± 600 K. That means the sweating crater contributed about 38% the amount of water contributed by the grains model. The water-release begins at 100±30 s, which means the sweating crater started contributing about half-way through the data collection period.

The prompt OH mass ($M_{OH,prompt}$) fitted result was only 24 g. This amount of mass is a tiny fraction compared to the mass of water in the lofted grains ($M_{H_2O,grains}$), which is consistent with our expectations. Since OH is highly reactive, the amount of OH present in the regolith was expected to be much less than the other mass parameters. Still, this relatively tiny amount of OH mass was enough to have a significant effect on the simulated OH band strength; the maximum contribution of the prompt OH signal is comparable to the maximum contribution of the grains model (both $\sim 0.8\ W/\mu m\ sr\, m^2$). However, the prompt OH band strength contribution occurs earlier than that of the other two models; this will explained in more detail later. The temperature of the OH particles promptly released ($T_{OH,prompt}$) resulted in 1080 ± 180 K. This result agrees with measurements of the plume temperature of about 1,000 K [18].

The overall large uncertainties in the OH observational data do have a significant effect on the simulated band strength. We describe the uncertainty of the OH measurements as *large*, applicable to our analysis, in the sense that we need large variations in our fitted parameter values in order to generate changes similar in magnitude to the data-uncertainty. The confidence intervals of the grains parameter values were between 25 and 82%. The prompt OH model was the best constrained model, with confidence intervals ranging between 8 and 17%.

On the other hand, the sweating crater model was the least constrained model. The uncertainty of the mass parameter ($M_{H_2O,sweat}$) is $\sim$ 100%, so we were not able to be sure if the physics represented by the sweating crater model were present in the LCROSS mission or not. Furthermore, because $M_{H_2O,sweat}$ is only about 40% that of $M_{H_2O,grains}$, and the *sweating* mechanism only becomes active after about 100 s post-impact, the model's contribution to the simulated band strength is relatively weak. As a matter of fact, when fitting the models to altered observational data sets, many of the sweating crater contributions were weak, or sometimes even negligible, similar to the contribution of the sweating crater model shown in Fig. 5.2. This will be discussed in more detail later in this chapter. However, we concluded that the resulting OH contribution from the sweating crater is much less than the other two models. The sweating crater model was not an essential process to characterize the OH observations (at least for the four minutes after Centaur's impact) and the OH band strength can be well represented by the prompt OH and grains models alone.

The final simulated OH band strength signal is shown in Fig. 6.1, along with other features and results from the fit. The contents of Fig. 6.1 will be explained in order of calculation. The black squares are the experimental data and the error bars their respective uncertainties. The thin faded lines in the background are all of $[Results2]_l$, the fits to the randomly altered data sets. These lines will be referred

Table 6.1: Characteristics of the curves that best fit the band-strength data. Grains heating model utilizing olivine as the dirt material.

Model	**Parameter**	**Parameter Value**
Grains (olivine)	$M_{H_2O,grains}$	800 ± 200 kg
	f_v	11 ± 9 %
	α	0.11 ± 0.07
Sweating Crater	$M_{H_2O,sweat}$	300 ± 300 kg
	$T_{H_2O,sweat}$	1800 ± 600 K
	t_{sweat}	100 ± 30 s
Prompt OH	$M_{OH,prompt}$	24 ± 2 g
	$T_{OH,prompt}$	1080 ± 180 K

to as the *single fits*. The red line is the average of all the single fits and will be called OH_{mean}. The blue line is the result of the LCROSS simulation using the average parameter values from Table 6.1 as inputs. The blue line will be referred to as *the simulation with averaged coefficients*, or just the OH_{LCROSS} curve. The three dashed lines are each model's contribution to OH_{LCROSS} curve — the final simulated OH band strength. In other words, OH_{LCROSS} is the sum of the three dashed lines.

The prompt OH model makes the highest contribution at early times (<15 s) of the simulation, and it is essential to describe the abrupt rise in the OH signal immediately after Centaur's impact. The other physical processes investigated have time delays that are inconsistent with such early observations. After the prompt OH contribution dies off, the grain model makes the largest contribution to the simulated signal throughout the remainder of the simulation. As described before, the sweating crater model had a relatively weak contribution, but still helps represent the later observations, reaching a maximum contribution of about 30% that of the total simulated OH signal.

An important feature to notice in Fig. 6.1 is the discrepancy between the OH_{mean} and the OH_{LCROSS} curves. The difference is most pronounced in the 10

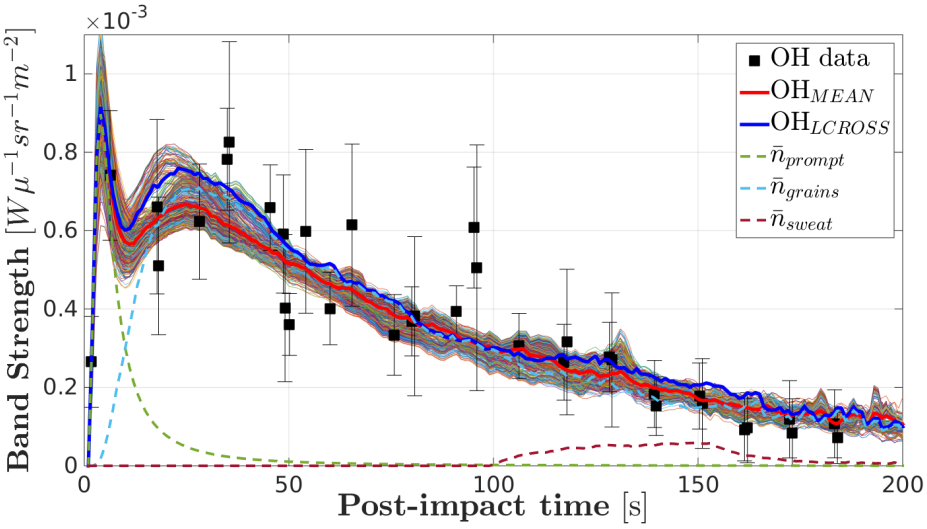

Figure 6.1: The black squares represent the LCROSS OH data considered for the analysis. The thin lines on the background (single fits) are all of $[Results2]_l$. OH_{mean} is the average of the single fits. OH_{LCROSS} is the result of the LCROSS simulation with Table 6.1 values as inputs.

to 50 seconds interval, where the OH_{LCROSS} is edging near the top of the single fits band rather than staying in the middle close to OH_{mean}. Even though their difference is not very big (about 13%), it is significant enough to raise concerns about the results. We expected these curves to be similar because OH_{LCROSS} represents the average parameter values of the single fits, and OH_{mean} is the average of the single fits. This discrepancy between OH_{LCROSS} and OH_{mean} appears to have two contributing reasons: the linear interpolation of a non-linear space in the discretization of the shape-defining parameters, and the existence of two or more families of solutions.

As described in Section 5.1.2, we discretized the shape-defining parameters utilizing the curves bank, and then averaged the parameter values from the single fits results. By averaging two or more curves (i.e. the single fits), we essentially interpolate between the parameter values defining the averaged curves. However, if

the parameter space is not linear, the curve from averaging single fits (e.g. OH_{mean}) may not be equivalent to the curve obtained from running the simulations with the averaged parameter values (e.g. OH_{LCROSS}).

We investigated the interpolation issues for the prompt OH and grain models — the two significant models where the discrepancy occurs. Interpolating indeed causes small differences between averaging pre-computed curves and actually running the LCROSS simulation with the parameter value that is to be interpolated. The grain model showed larger discrepancies when values were being interpolated, probably because of the interpolation of two parameters (α and f_v) rather than interpolating just one parameter as in the prompt OH model (T_{OH}). The larger discrepancies were in the order of 5%. In theory, this issue can be simply addressed by adding more cases into the curves bank and effectively having a denser parameter space. However, we tried addressing the issue this way, but refining the discrete parameter space did not decrease the difference between OH_{mean} and OH_{LCROSS} (the red and blue curves in Fig. 6.1). Therefore, interpolation and coarse discretization alone do not appear to cause the discrepancy.

The second contributing cause to the discrepancy in question may be the existence of multiple *modalities* of solutions in the results. This could also be thought of as two families of solutions. Hints as to the existence of different modalities can be observed in Fig. 6.1. There are appreciable gaps in between bands of single fits around twenty seconds post-impact. The effect of possible multiple modalities is clearly shown when we perform the whole fitting process, but we only consider one source of OH: the grains model. That is, the only source of OH in the LCROSS simulation is the grain model, and we do not consider any contributions from the prompt OH or sweating crater model. Results of such analysis are shown in Fig. 6.2. Fitting only the grains model to the data distinctly shows the two bands of solutions arising from the individual fits. As the experimental data is randomly altered within

the data error bars (in order to find the confidence intervals for the grain model fitting parameters) two different families of curves that *best* represent the experimental data arise. The resulting parameter values defining the single fits jump between two parameter values, rather than spreading around a single parameter value.

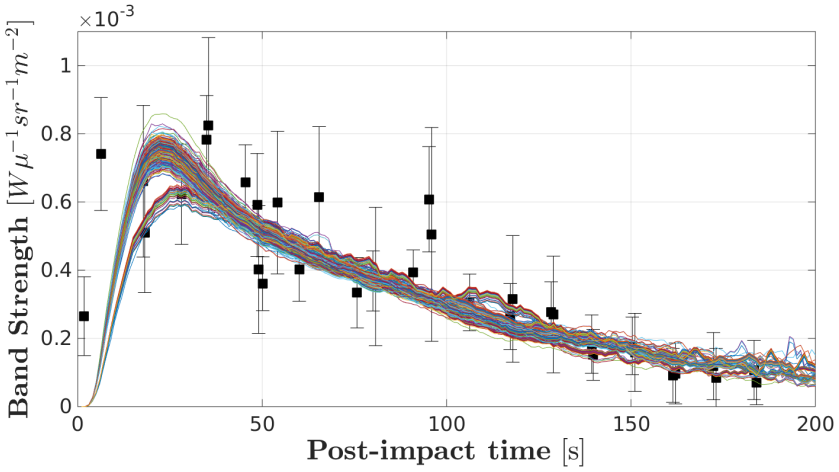

Figure 6.2: OH band strength data fitted with grains model only. Ignoring the prompt OH and sweating crater models in the fitting process distinctly shows the rise of at least two families of solutions.

We examined the phenomenon of multiple modalities present in Fig. 6.1 by looking at the histograms of results for the grains parameters. These histograms are shown in Fig. 6.3. Rather than seeing an approximately normal distribution around one parameter value, results cluster around different values. For example, the results of f_v cluster around 8% and 30%, without picking the intermediate values of 20%. The consequence is that the final averaged parameter values are essentially the result of averaging among the different families of solutions, rather than averaging among adjacent cases in the curves bank. In the f_v example mentioned above, this would be equivalent to averaging the 8% and 30% curves, as if these were the only values available in the curves bank, and ignoring all the in-between curves. The linear interpolation that implicitly occurs by averaging results (i.e. the discretization

of the parameter space) is effectively coarse. For this same reason, adding more curves to the bank (i.e. refining the discretization) does not help to reduce the gap between OH_{mean} and OH_{LCROSS}. Additional curves do not extinguish the existence of modalities, and the effective interpolation is still coarse.

On the other hand, the prompt OH model does have an approximately normal distribution around its average parameter values (Fig. 6.4). The distributions of the prompt OH results explain why this model was the best constrained model, having the narrowest confidence intervals percentage-wise. For the sweating crater model, the shape-defining parameters also show multiple modalities (Fig. 6.5). However, as mentioned before, the results of $M_{H_2O,sweat}$ clearly lean towards the relatively low-value results, resulting in weak or even negligible contributions.

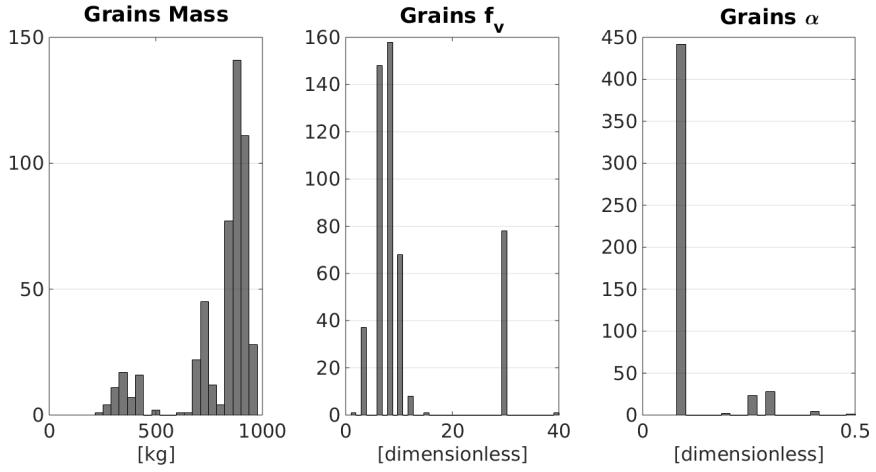

Figure 6.3: Histograms of grain model parameter results. Results cluster around different values rather than spreading out around a single value.

One explanation of why multiple families of solutions occur is that there might be a few key data points that are very significant in defining the characteristic shape of the OH observations. For both cases (the fit considering all three models and the fit considering the grains model only) the difference between the families is noticeable within the first fifty seconds of the observations. After that, all single fits

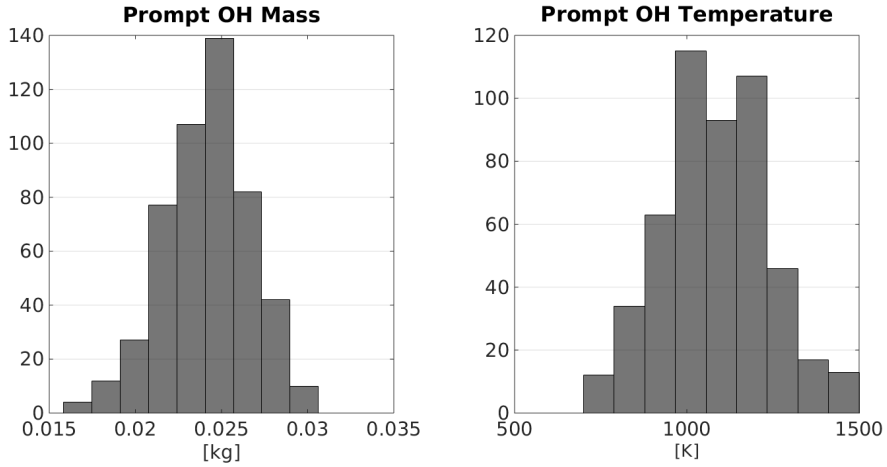

Figure 6.4: Histograms of prompt OH model parameter results. Distribution of results show an approximately normal distribution which results in the best constrained model.

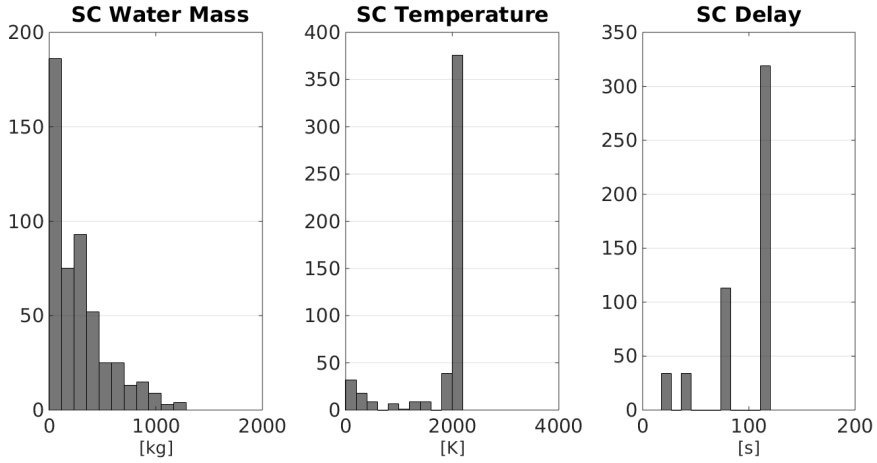

Figure 6.5: Histograms of sweating crater parameter results. The distribution of total amount of water shows leans towards relatively low values. The sweating crater contribution to the simulated OH band strength is altogether relatively weak.

blend into the same band. Therefore, there might be certain combinations of altered data points within the 10-50 s interval that force the choice of parameter values to flip between the modalities. Potentially, when the data points between 10 to 50 s all happen to be varied to higher values, the experimental data is better explained

with a more spiky grains curve. On the other hand, if the 10-50 s points all happen to be varied to lower values, the OH observation might be represented better with a flatter curve shape. Therefore, we observed the two distinct shapes in Fig. 6.2.

The result of multiple families of solutions arising from the fitting process is significant. First, the families of solutions cause a larger spread in the results of the grains' parameters fits (Fig. 6.3) that result in relatively high uncertainty in their values. Also, the modalities show the method is not completely robust to constrain the problem — the result may not have a unique solution. If this is the case, we would need to consider more information in order to properly constrain the grains model and resolve the parameter values between the multiple modalities. This additional information could be in the form of additional LCROSS data.

Alternatively to consider extra sets of data, we could try different and even multiple measures of error to asses the quality of the fits. We utilized $SSWR$ as the measure for goodness of the fit, but an example of an alternative measure can be the coefficient of determination (R^2) [19]. It might be possible that one of the families of curves is not relevant when considering alternative measures of the fit. If this is the case, we could and should select parameter values that are consistently prominent to be the final result. This possibility is suggested by the bias between the modes seen in Fig. 6.3; even though multiple solutions are noticeable, there are *strong* peaks that appear to be more probable than the others.

We could also increase the complexity of the models to see if more sophisticated models allow us to distinguish between the families of solutions. However nothing guarantees extra complexity will result in a unique solution. Furthermore, this may counterproductively introduce more unknown parameters into the problem.

Although we were not able to constrain all parameters, we found the interesting existence of multiple solutions. This feature of data fitting is not unique to this problem. In our process, we could have defined the fit of the original OH data

(*Result*2 shown in Fig. 5.2) as our final answer. After all, this set of values are the result that best represent the LCROSS OH observations. However, doing so would have neglected the fact that different sets of parameters-values generate acceptable results. Even though the main goal of varying the OH data and repeating the fitting process was to find confidence intervals on the fitted parameters, the emergence of multiple solutions is an interesting result.

The occurrence of multiple solutions is an expression of our models' limitations — we were not able to fully constrain the models. Knowing our modeling limitations may help guide the necessary areas of improvement. The fitting method served as a bridge between the experimental observations and the computational models. Through the fitting process, we connected the LCROSS observations to the computational methods to learn more about the nature of the mission. On the other hand, using the fitting method and the OH data, we validated some of our numerical models and learned about the limitations of our simulation.

Even though we did not completely constrain the problem, there are some conclusions we can draw from the results. First, the prompt OH model or a similar fast mechanism is necessary to characterize the early observations. Also, we concluded the sweating crater is not indispensable to characterize the data. Because the models were not completely constrained, we cannot conclude that the sweating crater effect was either existent or non-existent, but we proved that it is not essential to constrain the observations. Maybe all the nearby water got lofted by the Centaur's impact, and even though the impact generated a hot crater, there was no nearby water available for sublimation.

6.2 Pyroxene Results

So far, all the results presented were obtained utilizing olivine as the inclusion material in the grain heating model. However, as mentioned in Section 4.1.2, we

also calculated optical properties for ice grains containing pyroxene inclusions with the goal of comparing well constrained results among the two choices of dirt material. Since the models were not fully constrained for either olivine or pyroxene, we focused on the olivine results to illustrate the analysis and discussion. The fitted parameter values for pyroxene are summarized in Table 6.2. The conclusions stated above and qualitative results were the same for both materials. However, the pyroxene grains model required more ice to be lofted by Centaur's impact-plume (1000 kg compared to 800 kg for olivine) and also required grains to have more dirt inclusions (20% f_v rather than 11% for olivine). The average probability ratio of direct ice to vapor photodissociation (α) was consistent among pyroxene and olivine results.

Running the fitting method with pyroxene dirt inclusions resulted in an even weaker sweating crater contribution. The amount of water sublimated from Centaur's hot crater when using pyroxene inclusions is of about one third (110 kg) that of the sweating crater results when using olivine inclusions (300 kg). The shape-defining parameters of the sweating crater had consistent results among pyroxene and olivine results.

The prompt OH model had consistent results in both of its parameters. The amount of OH released was about 24 g with a temperature of about 1,000 K for both choices of dirt material. Consistent results in the parameter values of the prompt OH model (regardless of the dirt material choice) were expected since the prompt OH model is most prominent when the grains model is not. The prompt OH model was the best constrained mechanism for both choices of dirt material.

As mentioned before, the choice of grain material did not change the overall qualitative results, but did have some impact on the fitted parameter values. A more realistic scenario entails having a model with pyroxene-inclusions and olivine-inclusions grains, or having grains with olivine *and* pyroxene inclusions. Both of these options could be explored in future work.

Table 6.2: Characteristics of the curves that best fit the band-strength data. Grains heating model utilizing pyroxene as the dirt material

Model	Parameter	Parameter Value
Grains (pyroxene)	$M_{H_2O,grains}$	1000 ± 300 kg
	f_v	20 ± 20 %
	α	0.10 ± 0.07
Sweating Crater	$M_{H_2O,sweat}$	110 ± 180 kg
	$T_{H_2O,sweat}$	1600 ± 700 K
	t_sweat	90 ± 40 s
Prompt OH	$M_{OH,prompt}$	23 ± 3 g
	$T_{OH,prompt}$	1110 ± 160 K

6.3 Sources of Error

There are multiple potential sources of error influencing the presented results. Measures were taken throughout the analysis to minimize the effects of these potential errors, quantify uncertainties, and make the best use of the OH band strength data. The error bars on the experimental data account for the statistical errors of processing the data; processing the data was performed by collaborator Dr. Anthony Colaprete. The statistical processing yielding the experimental error bars itself addresses uncertainty from the measurements and the instrumentation. In the estimation of the band strength from the numerical model, there is uncertainty in the assumptions for the *g-factor* calculation and the estimated value of the *g-factor* itself (Appendix A). Uncertainties from the *g-factor* were not directly addressed, and might have caused a proportional bias in the results. More importantly, all numerical models had simplifying assumptions. These assumptions include dirt constituents of a single material (olivine or pyroxene), constant water release rate from the sweating crater, release mechanisms of the prompt OH, etc. Such simplifying assumptions were at least reasonable, and aimed to represent average properties in the complex problem. However, we cannot guarantee these simplifications did not

affect the results: different or more refined physical models could yet be explored.

Chapter 7

Conclusions

The LCROSS mission launched by NASA in 2019 successfully confirmed the presence of water in the moon. However, questions about the characteristics of the Moon's permanently shadowed areas still remain. The hydroxyl band strength data observed during the LCROSS mission had not been analyzed in detail before, and may be useful in learning more about the polar region of the Moon. We utilized these data to learn about the hypothesized OH producing mechanisms that were potentially observed by the LCROSS instrumentation.

We simulated the hydroxyl band strength data utilizing a Monte Carlo simulation. Our simulating code was based on Heldmann et al.'s (2015) previous work, but included improvements on the representation of the physics and new OH-producing sub-models. The three hypothesized OH-producing models are the photodissociation of water from ice-containing grains in the impact-plume, photodissociation of water sublimated from Centaur's hot impact-crater, and OH radicals originally present in the Moon's regolith that were ejected by the first spacecraft-impact.

In order to constrain unknown parameter values for the OH producing models, we fitted the computational results to the OH observations. In the first part of

the fitting method, we discretized the parameter values of the three OH producing models. Then, using a least-squares fit, we fitted the combinations of parameter values to the observational data by scaling the contributions of the OH-producing models to the simulated band strength, and looked at the combination that best represented the OH observations. In the second part of the fitting method, we repeated the first-part of the process multiple times; each time we repeated the process, we randomly varied (using a Gaussian distribution) the observational data within the data's error bars in order to see how these variations affected our results. Finally, we utilized the effects varying the observational data had in our results to estimate confidence intervals in the fitted parameter values.

The fit of the observational data was not conclusive. Multiple solutions emerged from the fitting process, and therefore, we were not able to completely constrain the models. Still, there are some conclusions that were drawn from the results. A *fast* OH-producing mechanism such as the prompt OH model is necessary to characterize the early OH observations. The sweating crater model (water vaporizing from the hot impact-crater) had a relatively weak contribution, and is not essential to the representation of the observed OH signal. In order to further constrain the models, additional LCROSS data are necessary. Finally, the fitting method could potentially be used to explore the possibility of multiple solutions in a given problem.

7.1 Future Work

Much of the potential continuation of this work has already been mentioned throughout the discussion of the results. Probably the most important future step is to finish constraining the proposed models. The simplest next approach is to consider different and/or multiple measures (such as R^2) to determine the quality of the fits. Different measures for goodness of the fit might filter out some of the multiple

solutions and unveil parameter-values that are consistently prominent as the best results.

Another option to better constrain the nature of the impact event is to consider additional LCROSS data. The OH data from the VSP examined herein were both noisy and limited. Considering additional observational data would introduce additional information from the observations. This approach might be more robust than just considering different measures for goodness of the fit which are just statistical tools that do not necessarily add information. For example, we could utilize the data from the sun-looking near-infrared spectrometer NSP2 [5] in the least square minimization.

After constraining current models, we could consider increasing their complexity. For the grains models, we could introduce grains with a distribution of f_v. We could also consider α as a function of f_v, dirt material, etc. For the prompt OH model, we could consider that some OH was trapped within the water-ice and got ejected as water sublimed from the grains; we could develop a mechanism-model that accounts for such possibility. For the sweating crater model, we could have a non-constant vapor release rate, and/or vary the release temperature of water ($T_{H_2O,sweat}$). Of course, before increasing the complexity of any of our mechanisms we would have to evaluate how helpful and revealing additional complexities can be, and decide if these complexities are worth exploring.

Another significant endeavor would be to consolidate our work with previous studies. As mentioned in Section 4.2.1, many of the parameters in the simulation were set to nominal values from Heldmann et al.'s previous work. However, we modified some of the mechanisms used in their studies and introduced new models into their simulation approach. These new models introduced additional representative particles and parameters that may or may not affect Heldmann et al.'s results. A future study simultaneously constraining all parameters would be more consistent

and physically meaningful than two separate studies constraining different sets of parameters. Pursuing this will also be a way to consider additional LCROSS data to further constrain our results. However, pursuing this route might be limited by the large number of parameters that will have to be considered. Therefore, a study to determine importance of each parameter and narrow down the number of parameters might be desirable, if not necessary.

One option to effectively accomplish a sensitivity study for a large number of parameters and narrow down the number of dependencies is to do a Monte Carlo Sensitivity Analysis, described in detail by Strand and Goldstein [20]. The basic idea is to simultaneously vary all parameters randomly, choose a quantity of interest (QoI) related to the results of the simulation, and examine the relationship between a given parameter and the relationship of interest. The QoI is usually an experimentally measurable quantity. For our simulation as an example, we could choose the QoI to be the amount of OH at 35 s post-impact time — the time where the OH band strength observation had the largest magnitude. Then, we would pick a nominal case of parameter values based on expert knowledge, previous measurements, or another informed guess. Each parameter would have a range of variation with a distribution that depends on how confident we are on the guessed value of each parameter. From there, we would run the simulation multiple times randomly varying the parameter values — similar to our procedure that quantifies confidence intervals — and we would examine the relationship between the parameters and the QoI. The relationship between parameters and the QoI is quantified by statistical quantities like R^2 (also known as the *Pearson correlation coefficient*) or the *mutual information*. Using this method we can estimate the relative significance of parameters in a simulation. Alternatively, this method can show whether the parameters we are interested in constraining have a relationship to the experimental data.

Appendix A

g-factor Calculation

The Chamberlain g-factor, as described by Cageao et al. [16], relates the specific intensity (I) of a particular vibrational-rotational transition to the observed column abundance of the emitting molecule:

$$4\pi I = gn \tag{A.1}$$

where $4\pi I$ is the emitted flux (in Rayleighs) over 4π steradians, n is the column abundance along the observed path (#/cm^2), and g is the emission rate g-factor (photons/second).

Utilizing the relationship in Eq. (A.1), we estimated the apparent OH band signal at a point in time given the number of molecules in-view (inside the spectrometer's field-of-view) from our simulations. We achieved this by solving for the intensity, I, in Eq. (A.1). In order to compare our simulation results to the OH observational data, we additionally had to transform I from Rayleighs to band strength units, and divide by the spectrometer's wavelength ($\Delta\lambda$):

$$I = g \times n \times \frac{1}{4\pi} \times E_{OH} \times \frac{1}{\Delta\lambda} \tag{A.2}$$

$$\left[\frac{W}{(m^2)\,(sr)\,(\mu m)}\right] = \left[\frac{photons}{s} * \frac{\#}{m^2} * \frac{1}{sr} * \frac{J}{photon} * \frac{1}{\mu m}\right] \tag{A.3}$$

Where E_{OH} is the energy of a photon emitted by an OH molecule with $\lambda_{OH} = 309$nm

$$E_{OH} = \frac{hc}{\lambda_{OH}} \tag{A.4}$$

Having calculated I from the number of particles inside the instrument's field-of-view, we were able to compare our computational results to the LCROSS OH observations. The value of the g-factor used in our calculations was 3.8×10^{-4} based on Collaborator's Dr. Anthony Colaprete's suggestion.

Bibliography

[1] Jennifer L Heldmann, Justin Lamb, Daniel Asturias, Anthony Colaprete, David B Goldstein, Laurence M Trafton, and Philip L Varghese. Evolution of the dust and water ice plume components as observed by the lcross visible camera and uv–visible spectrometer. *Icarus*, 254:262–275, 2015.

[2] Anthony Colaprete, Peter Schultz, Jennifer Heldmann, Diane Wooden, Mark Shirley, Kimberly Ennico, Brendan Hermalyn, William Marshall, Antonio Ricco, Richard C Elphic, et al. Detection of water in the lcross ejecta plume. *science*, 330(6003):463–468, 2010.

[3] W C Feldman, S Maurice, AB Binder, BL Barraclough, RC Elphic, and DJ Lawrence. Fluxes of fast and epithermal neutrons from lunar prospector: Evidence for water ice at the lunar poles. *Science*, 281(5382):1496–1500, 1998.

[4] WC Feldman, WV Boynton, BM Jakosky, and MT Mellon. Redistribution of subsurface neutrons caused by ground ice on mars. *Journal of Geophysical Research: Planets*, 98(E11):20855–20870, 1993.

[5] Kimberly Ennico, Mark Shirley, Anthony Colaprete, and Leonid Osetinsky. The lunar crater observation and sensing satellite (lcross) payload development and performance ináflight. *Space science reviews*, 167(1-4):23–69, 2012.

[6] P Rousselot, J Clairemidi, F Vernotte, and G Moreels. A direct way to observe

the photodissociation of water vapor in a cometary coma consists to detect the oh prompt emission. this emission is shifted of sa= 4 nm with respect to the oh 309 nm fluorescence band. the extended data set obtained with the three-channel spectrometer on-board vega 2 reveals at short distance of the nucleus (ie less than 600 km) an excess of emission on the right wing of the oh band which may be interpreted as being mainly due to prompt emission. *Asteroids, Comets, Meteors*, pages 525–528, 1991.

[7] WF Huebner and J Mukherjee. Photoionization and photodissociation rates in solar and blackbody radiation fields. *Planetary and Space Science*, 106:11–45, 2015.

[8] CY Wu and FZ Chen. Velocity distributions of hydrogen atoms and hydroxyl radicals produced through solar photodissociation of water. *Journal of Geophysical Research: Planets*, 98(E4):7415–7435, 1993.

[9] Warren J Wiscombe. *Mie scattering calculations: Advances in technique and fast, vector-speed computer codes*, volume 10. National Technical Information Service, US Department of Commerce, 1979.

[10] T Mukai. Analysis of a dirty water-ice model for cometary dust. *Astronomy and Astrophysics*, 164:397–407, 1986.

[11] Grant H Heiken, David T Vaniman, and Bevan M French. Lunar sourcebook-a user's guide to the moon. *Research supported by NASA,. Cambridge, England, Cambridge University Press, 1991, 753 p. No individual items are abstracted in this volume.*, 1991.

[12] TI Quickenden, AJ Matich, MG Bakker, CG Freeman, and DF Sangster. The effect of temperature on the luminescence from electron-irradiated h2o ice. *The Journal of chemical physics*, 95(12):8843–8852, 1991.

[13] PA Gerakines, Marla H Moore, and Reggie L Hudson. Carbonic acid production in h_2o: Co_2 ices. uv photolysis vs. proton bombardment. *Astronomy and Astrophysics*, 357:793–800, 2000.

[14] Paul O Hayne, Benjamin T Greenhagen, Marc C Foote, Matthew A Siegler, Ashwin R Vasavada, and David A Paige. Diviner lunar radiometer observations of the lcross impact. *Science*, 330(6003):477–479, 2010.

[15] C M Pieters, JN Goswami, RN Clark, M Annadurai, J Boardman, B Buratti, J-P Combe, MD Dyar, R Green, JW Head, et al. Character and spatial distribution of oh/h2o on the surface of the moon seen by m3 on chandrayaan-1. *science*, 326(5952):568–572, 2009.

[16] RP Cageao, YL Ha, Y Jiang, MF Morgan, YL Yung, and SP Sander. Calculated hydroxyl a2 x2π (0, 0) band emission rate factors applicable to atmospheric spectroscopy. *Journal of Quantitative Spectroscopy and Radiative Transfer*, 57 (5):703–717, 1997.

[17] The MathWorks inc. lsqcurvefit. `https://www.mathworks.com/help/optim/ug/lsqcurvefit.html` Accessed: 2019-04-27.

[18] G Randall Gladstone, Dana M Hurley, Kurt D Retherford, Paul D Feldman, Wayne R Pryor, Jean-Yves Chaufray, Maarten Versteeg, Thomas K Greathouse, Andrew J Steffl, Henry Throop, et al. Lro-lamp observations of the lcross impact plume. *Science*, 330(6003):472–476, 2010.

[19] Nico JD Nagelkerke et al. A note on a general definition of the coefficient of determination. *Biometrika*, 78(3):691–692, 1991.

[20] James S Strand and David B Goldstein. Global sensitivity analysis for dsmc simulations of hypersonic shocks. *Journal of Computational Physics*, 246:184–206, 2013.